**Remarks on Application of VMEC and PROCTR
to the Wendelstein 7-AS Experiment**

Hiroshi Yamada*, Joachim Geiger, Ulrich Stroth,
Arthur Weller, Herb C. Howe**

IPP III / 194   Februar 1994

IPP

MAX-PLANCK-INSTITUT FÜR PLASMAPHYSIK

85748 GARCHING BEI MÜNCHEN

MAX-PLANCK-INSTITUT FÜR PLASMAPHYSIK

GARCHING BEI MÜNCHEN

Remarks on Application of VMEC and PROCTR
to the Wendelstein 7-AS Experiment

Hiroshi Yamada*, Joachim Geiger, Ulrich Stroth,
Arthur Weller, Herb C. Howe**

IPP III / 194   Februar 1994

MAX-PLANCK-INSTITUT FÜR PLASMAPHYSIK
GARCHING BEI MÜNCHEN

Remarks on Application of VMEC and PROCTR to the Wendelstein 7-AS Experiment

Hiroshi Yamada*, Joachim Geiger, Ulrich Stroth,

Arthur Weller, Herb C. Howe**

Abstract

This report describes the application of the VMEC (Variational Moments Equilibrium Code) and PROCTR (PRedictOr Corrector TRansport code) numerical codes to the W7-AS experiment. The different versions of VMEC, each of which has been used for W7-AS and CHS (National Institute for Fusion Science, Nagoya, Japan), were compared to confirm their reliability and performance, and successfully benchmarked. The PROCTR code set was installed in the Wendelstein-VAX cluster. Its potential in experimental interpretation and theoretical analysis was demonstrated for coordinate inversion based on full 3-D geometry, power balance analysis and time-dependent transport simulation. The benchmark tests of tools for finite-β equilibrium and power balance analysis are a prerequisite for the joint profile and configuration database for stellarators which has just been started. We successfully recognized the compatibility of the schemes used on W7-AS and CHS.

* on leave from National Institute for Fusion Science, Nagoya 464-01, Japan

** Oak Ridge National Laboratory, Oak Ridge, TN 37831, USA

1. Introduction

Stellarators and tokamaks have been studied since the beginning of magnetic fusion research. Axisymmetric (2-D) approaches in theoretical studies have been quite successful for tokamak configurations. Although similar approaches have certainly benefited stellarator studies, their applicability is often limited owing to the intrinsic complexity of the 3-D geometry of stellarators. Recently, however, rapid advances in numerical computation have been made and systematic schemes based on the 3-D theory have been obtained. These numerical tools have greatly facilitated interpretation of experimental observation as well as provided reliable prediction from theory.

In this report, we comment on the application of two powerful numerical codes: VMEC (Variational Moments Equilibrium Code) [1] for free-boundary finite-β equilibrium and PROCTR (PRedictOr Corrector TRansport code) [2] for profile analysis and time-dependent transport simulation. The VMEC code has already been widely used for a variety of stellarators and even for tokamaks, and the linkage to other numerical codes has been readily accomplished. The PROCTR code is essentially a 1-D transport code, but physical observations can be transformed between full 3-D and 1-D by coordinate inversion using the full 3-D geometry given by VMEC. Time-dependent simulations with various models can be done and profile analysis such as chord tracking and power balance analysis is also available. In the CHS and ATF experiments, self-consistent finite-β equilibria have been routinely calculated from experimental observations using VMEC and PROCTR [3,4]. Also power balance analysis has been done simultaneously in this analysis flow [4,5]. Reconstructed equilibrium with VMEC has also been discussed with the electron temperature and density profiles in the W7-AS "advanced stellarator" [6].

We have started a joint stellarator global database [7], which will be extended to a more comprehensive profile and configuration database. The main contributers are ATF (ORNL, USA), W7-AS (IPP, Germany), Heliotron E (Kyoto Univ., Japan) and CHS (NIFS, Japan). These comparative studies are of great importance for understanding present experiments, particularly, configuration effects on transport and MHD characteristics, and efficient

conduction in next-generation experiments: LHD and W7-X. The benchmark test of the numerical code employed is a prerequisite to establishing a reliable database. We checked the validity of the analyses used for the computation of finite-β equilibria and the power balance in W7-AS and CHS by doing benchmark tests.

2. Equilibrium Study with VMEC

2.1 Comparison of W7-AS with CHS

Compared with conventional stellarator/heliotron/torsatron configurations, W7-AS [8] and CHS [9] have certain distinct features. W7-AS is a partially optimized advanced stellarator and CHS is a low-aspect-ratio heliotron/torsatron. They occupy opposite positions in current stellarator/heliotron/torsatron experiments, while having the common characteristic of complex Fourier harmonics of the magnetic field, which presents difficulties in theoretical approaches. W7-AS has improved equilibrium properties due to reduction of the Pfirsch-Schlüter currents, while CHS makes use of a large Shafranov shift for efficient generation of a magnetic well which stabilizes the interchange mode. Figure 1 shows the Shafranov shift Δ [10] of the standard configurations in W7-AS at low ι (R_{ax}=1.978m, a=0.181m, ι_0=0.342, ι_a=0.345, B_v=50G corresponding to B_t=1.25T) and in CHS (R_{ax} = 0.921m, a=0.192m, ι_0=0.307, ι_a=1.10). Here R_{ax} is the major radius of the magnetic axis at ϕ=0 (W7-AS: triangular cross-section, CHS: highly vertically elongated cross-section). The pressure profile is given as p = $p_0(1-\psi)^2$, where ψ is the toroidal flux function for both configurations. It should be noted that the vacuum magnetic axis is not necessarily located at the center of the last closed flux surface. Since Δ is estimated from the stellarator expansion as $\Delta=\beta_0 A_p a/\iota_a^2$, a crude discussion suggests that the Shafranov shift of W7-AS ought to be 5 times larger than that of CHS for the above parameters. However, the Shafranov shifts are almost the same, which indicates the significant improvement achieved by partial optimization of the W7-AS configuration. The equilibrium β-limit is comparable in the two configurations. It should also be pointed out that the configuration with higher rotational transform gives a higher equilibrium β-limit in W7-AS and that vertical-field compensation may increase the β-limit in both configurations.

In VMEC, physical quantities are decomposed into Fourier components in a poloidal angle θ and a toroidal angle ζ. Careful attention should therefore be paid to the number of modes used. Figure 2 shows the vacuum flux surfaces calculated in CHS by VMEC with different mode numbers. There is no substantial difference and the discretization with m=0~3 and n=-3~3 (the total number of Fourier modes is 25) is sufficient for CHS. In the case of W7-AS, a more sophisticated treatment is required to get a consistent equilibrium. Figure 3 indicates that the expansion with m=0~5 and n=-4~4 is not sufficient. A mode number of at least 128 (m=0~7 and n=-8~8) is necessary to obtain a sufficiently high quality for experimental diagnostics. This strict requirement is attributed to several leading harmonics of the magnetic field and low shear.

2.2 Benchmark Test of Codes

Although the theoretical model is identical, various versions of VMEC have been developed. The numerical treatments for the version used for CHS and that for W7-AS are different. The latter is specifically named NEMEC because of its connection with the NESTOR code. The main differences are the schemes for calculating the vacuum magnetic field and the implementation of the numerical solution of the Neumann problem [11] connected with the magnetic field outside the plasma. While VMEC utilizes prepared grid data of the vacuum magnetic field with interpolation, NEMEC calculates the vacuum magnetic field by means of the Biot-Savart law for every iteration.

A benchmark test was performed to check the reliability and performance of the two codes. The W7-AS configuration used in this test is generated by using only the modular coil system, and the pressure profile is given by $p = p_0(1-\psi)$. The grid data points for VMEC are given every 1.8cm in the R-direction, every 2.6 cm in the Z-direction and every 3 degrees in the ζ−direction, which results in the expansion of the effective area of one period to 51(R)×51(Z)×24(ζ) grid points. The magnetic surfaces agree quite well with each other for the vacuum case (see Fig.4) and tolerable agreement is achieved for the high-β case with $<\beta>$ =

2.5% (see Fig.5). The slight disagreement in the high-β case can be reduced by using a finer grid. Other physical quantities such as the rotational transform and Shafranov shift (see Fig.6) also show good agreement. Although the agreement between the two codes is sufficient for interpreting experimental observations, theoretical analysis calls for stricter agreement. The Fourier components of the magnetic field are important in the calculation of neoclassical transport. In the case shown in Fig. 5, quite good agreement is obtained even for magnetic field components with a small amplitude (see Fig.7). Although the results from the two codes demonstrate their individual reliabilities, they differ in performance. The number of iterations necessary for convergence is essentially the same in the two codes (see Fig.8 (a)). The CPU time required with VMEC is roughly 4 times as short as that with NEMEC (see Fig.8(b)). Since the stricter treatment, which requires more CPU time, is necessary for W7-AS, VMEC has an advantage. However, it should be noted that NEMEC needs a smaller memory size for execution than VMEC (NEMEC: 2.2MB and VMEC: 5.1MB under the present conditions). Also NEMEC has succeeded in reducing the CPU time requirement by a factor of 50% by also using a predefined vacuum magnetic field grid like VMEC with negligibly higher memory requirements.

2.3 On Application of Output from VMEC

The equilibrium obtained with VMEC is quite useful and the description of the magnetic field structure in VMEC is becoming standard for 3-D equilibrium and transport analysis. A variety of computational codes employ VMEC output. For example, the interface has been quite well arranged for the DKES code [12] (estimate of neoclassical transport coefficient). PROCTR contains an interface for using VMEC output and providing input to VMEC for recalculation. Bootstrap current can be calculated by standard neoclassical theory (from 1/ν to plateau regimes) with the KSPBSC code [13] using results from VMEC. The MHD stability analysis code, KSPDIAG [14], reads the VMEC output direct.

As an example of application of these codes, pressure-driven instability has been examined by using the Mercier criterion D_I (ideal interchange mode) and the stability criterion for resistive

5

interchange modes D_R [15] with KSPDIAG for W7-AS. Here positive values indicate stability for both criteria. Figure 9 shows D_I and D_R for the equilibrium obtained with VMEC in the benchmark test described in Sec.2.2. Since W7-AS is characterized by a vacuum magnetic well, the ideal interchange mode is stable as expected. The resistive interchange modes are also stable in this configuration owing to deepening of the magnetic well due to the Shafranov shift. In this survey, the vertical field is not employed and the plasma undergoes a significant outward shift. When the vertical field is applied to centralize the plasma in the vacuum vessel, the Mercier-unstable region appears in the peripheral region because the vacuum magnetic well is reduced by the vertical field. A peaked pressure profile ($p = p_0(1-\psi)^2$) can destabilize the ideal interchange mode for lower β values as well.

3. Transport Analysis with PROCTR

3.1 Examples of Application of PROCTR to Experiments

In addition to transport analysis, PROCTR includes convenient tools for the interpretation of experiments. Because of the complexity of 3-D flux surfaces, experimental observations are often hard to interpret. Coordinate inversion and chord tracking based on the 3-D geometry given by VMEC is possible with PROCTR. Soft X-ray signals which are line-integrated are analyzed as an example. Figure 10 shows the time evolution of soft X-ray signals with different thicknesses of the Be filter in an ECH discharge at 1.25T (#25395). While the profile detected with a 25μm filter is fairly peaked, the profile detected with no filter shows hollowness. These two profiles are inverted to 1-D (with respect to the flux surface coordinate) by using an appropriate finite-β equilibrium calculated with VMEC. The profile with the 25μm filter is well fitted to the magnetic flux surfaces and the detected emission is an indication of the plasma pressure. The two sides of the profile with respect to the magnetic axis coincide with each other (see Fig.11 (a)). In contrast, the profile with no filter cannot be fitted to a good 1-D profile (see Fig.11(b)). Since the emission measured without filter can contain much of the $K\alpha$ line radiation of oxygen, this result seems to be reasonable.

3.2 Benchmark Test of Power Balance Analysis

Local transport analysis of the power balance is fundamental to discussing confinement characteristics. We did benchmark tests of the schemes used in W7-AS [16] and CHS (PROCTR) to check their reliability and provide a basis for comparative studies. Two profile data sets were examined. The one is #18148 (discharge with 70GHz-ECH at 1.25T) of W7-AS and the other is #15653 (discharge with both 28GHz and 53GHz-ECH at 0.95T) of CHS. The exchanged input data consist of the electron temperature, electron density, ion temperature, neutral density and deposited power on a radial grid of 31 points, and the 3-D configuration. The convection multiplier is temporarily set at 5/2 and Z_{eff} is assumed to be 2 and spatially constant. In conclusion, remarkable agreement is found between the two cases. Figure 12 shows the electron heat diffusivity given by the two methods used in W7-AS and CHS. Figure 12 (a) also suggests that careful attention should be paid to the treatment of the geometry. When a simple circular geometry is considered, the local heat diffusivity becomes twice as large as with the correct treatment of the geometry.

The conventional treatment of the diffusive nature of the heat transport assumes that the local heat flux is proportional to the local temperature gradient in real space. The heat flux across flux surfaces can be given by the expression $\Gamma = P/V_p'<(\nabla\rho)^2>_\psi$, where the brackets denote the flux-surface average. In axisymmetric toroidal geometry with circular flux surfaces the term $V_p'<(\nabla\rho)^2>_\psi$ is identical to the flux surface area ($|\nabla\rho| = 1$). In a 3-D geometry, however, we have to pay careful attention to this geometrical factor in the flux average of the radial flux component. Figure 13 shows this geometrical factor for W7-AS and CHS. For the circular geometry, it is unity. When it is 2, the flux is overestimated by a factor of 2 if a circular geometry is assumed. With an increase of β, the outer flux surfaces are distorted and almost touch. At high β, $\nabla\rho$ therefore becomes large and the geometrical factor is enhanced. W7-AS has vertical elongation with a toroidally averaged ellipticity of around 2, which also enlarges the geometrical factor. Comparing the heat flux in this formula with the results from

neoclassical theory, the flux-surface-averaged gradient term seems to be artificial since it does not appear in the expression for the neoclassical heat flux. Attention should therefore be paid to geometry effects on transport in comparing different theories and particularly in comparing different devices.

3.3 Time-dependent Simulation with PROCTR

The temporal behavior of a discharge can be simulated by PROCTR, which includes time- and space-dependent models for the plasma hydrogenic ion, helium, and impurity densities, the electron and ion temperatures, the toroidal rotation velocity, and the toroidal current profile. PROCTR can be used to model actual stellarator discharges by using experimental data with appropriate conditions and assumptions [17]. The physical model in the code is examined by comparing predicted diagnostic measurements with experiment. A purely theoretical run is also possible.

Two NBI discharges in W7-AS were simulated. The one is #24595 (B_t=1.27T, ℓ_a=0.346) with slow ramping of the density up to $\bar{n}_e$=5×10^{19}m^{-3}. The other is the high-β discharge #25241(B_t=1.25T, ℓ_a=0.34, with the mirror ratio MR=-10% [18]) which is characterized by an extremely high density of up to $\bar{n}_e$=2×10^{20}m^{-3}. The simulation includes various physical models and assumptions which might not be justified. The primary uncertainty may be caused by the estimation of the power deposition of NBI. The beam heating profile calculated with PROCTR consists of two parts: the initial neutral deposition and the subsequent thermalization of the resulting fast ions. The plasma flux surfaces are assumed to be axisymmetric, circular toroids which approximate the actual 3-D surfaces . This assumption was checked, for ATF and CHS, by comparing the PROCTR model with a fully 3-D Monte Carlo deposition model. The initial neutral deposition profiles and shinethrough from the two models agreed well over a range of plasma density. For W7-AS, however, the axisymmetric-flux-surface assumption for the calculation may not be sufficient, because the distortion of the W7-AS surfaces is larger than in ATF and CHS and the field period is only 5. In the thermalization in PROCTR, fast ion orbits are not treated and the fast ions are assumed to slow

8

down on the birth flux surface with constant plasma parameters. Since the orbit of fast ions significantly deviates from flux surfaces in stellarators, the orbit loss and cx loss can be overestimated by PROCTR. For more accurate and reliable simulation, the power deposition process in W7-AS has to be checked with a 3-D Monte Carlo code. In particular, it should be treated more carefully in the low-density regime, where the thermalization process becomes dominant.

It should be noted that the results described in the following are examples of simulations and are quite sensitive to variations in the assumed plasma parameters. Careful comparison with experimental observation using various diagnostics is required to get a more conclusive picture.

Discharge #24595

Figure 14 shows the temporal behavior of the discharge. The dashed curves give the result of the transport simulation. The density rise during NBI is equal to the beam fueling rate. The neutral fluxes from the wall and gas puff are assumed to be entirely absorbed (100% reflection of the cx flux). The particle diffusion coefficient is assumed to be 15m^2/s for ρ<0.5 and to increase gradually to 30m^2/s towards the edge. The plasma recycling coefficient is varied by feedback to force the simulated line-average density to follow the measured density. The resulting recycling coefficient is <1 during the initial gas puff but then becomes unity during the NBI phase. This means that the rise in density is exactly equal to the fueling by thermalized fast ion, it being assumed that all of these ions are retained in the machine. The simulated stored energy is forced to follow the measured stored energy by varying the level of the anomalous electron heat conduction with a feedback algorithm. The thermal diffusivity of the electrons, χ_e, is given by the sum of a fixed radial profile $2+5\exp(-20(1-\rho))$ times a multiplier and the axisymmetric neoclassical conduction. The shape of χ_e is determined empirically, showing a large enhancement towards the edge. The thermal diffusivity of the ions is given by the Hinton-Hazeltine formula [19]. Although the helical ripple transport is not considered here, this assumption is valid in this simulation because of the high-density collisional plasma.

9

During the NBI phase, the multiplier for χ_e drops to a low value as the density increases, indicating that the anomalous χ_e becomes smaller. However, the total electron heat conduction loss is still much larger than the neoclassical loss at the end of the discharge. Also, the electron and ion heat conduction losses are approximately equal (see Fig.15).

In relatively low-density operation, unthermalized pressure due to fast ions can significantly contribute to the MHD equilibrium. When the neutral beam is injected tangentially as in W7-AS, unthermalized fast ions generate pressure parallel to the magnetic field. This results in pressure anisotropy. The stored energy W_{dia} in Fig.14 is the volume integral of the perpendicular pressure $(3/2 \cdot \int p_\perp dv)$, while W_{sdl} is that of the perpendicular and parallel pressures $(3/4 \cdot \int (p_\perp + p_{//}) dv)$. The former corresponds to diamagnetic measurement of the stored energy. The latter is related to Pfirsch-Schlüter currents. In the earlier phase of the NBI pulse, W_{sdl} is significantly larger than W_{dia} (W_{sdl}=4.4kJ and W_{dia}= 2.8kJ at 200 ms when $\bar{n}_e$=2.5×10^{19}m^{-3}) while they come closer to each other at the end of the discharge (W_{sdl}=5.0kJ and W_{dia}= 4.4kJ at 500 ms when $\bar{n}_e$=4.9×10^{19}m^{-3}). Since, in the case of W7-AS, the experimental measurement of W_{sdl} is greatly facilitated by a shearless configuration (see Appendix), clarification of this simulation is expected in the experiment.

Discharge #25241

When the same models that were used for #24595 are applied to #25241, the simulated time evolution of the line density follows the measured evolution. However, the simulated stored energy drops to very small values as the plasma density is increased. The final power balances show that all of the beam power is deposited in the electrons, transferred to the ions by collisions, and then transported out by ion heat conduction. .

As a next attempt, the ion heat conduction is set to the neoclassical value multiplied by 0.10 and the neoclassical electron heat conduction is turned off entirely. With these reductions, the simulated stored energy increases to almost the measured level (see Fig.16). Comparison between the actual and neoclassical heat transport levels at the final time indicates that the

10

simulated conductive heat loss is much less than the neoclassical level (see Fig.17).

Thus, in order to model this discharge, we have to assume that heat conduction is much less than the Hinton-Hazeltine neoclassical level, at least for ions. The power balance study also suggested that the enhancement factor above neoclassical ion heat conduction usually becomes smaller as the density increases. Obviously, in reality, transport cannot be less than the collisional level. There is therefore a possibility that the Hinton-Hazeltine neoclassical model cannot be blindly applied to the complicated flux-surface geometry in W7-AS, particularly, in high-density regime. In the case of very high density, the validity of the numerical model employed has to be clarified in detail.

4. Summary

In this report, we discuss a variety of applications of the VMEC and PROCTR numerical codes to W7-AS experiment. The different versions of VMEC, each of which has been used for W7-AS and CHS, are compared to confirm their reliability and performance, and successfully benchmarked. An example of stability analysis based on an equilibrium given by VMEC is introduced. The PROCTR code set was installed in the Wendelstein-VAX cluster. Coordinate inversion based on the full 3-D geometry, power balance analysis and time-dependent transport simulation were demonstrated with PROCTR. The complexity of 3-D has posed the problem of how to treat the flux-averaged gradient term and a measurement of the pressure anisotropy is proposed. Time-dependent simulation suggests that the Hinton-Hazeltine neoclassical model cannot be blindly applied to the complicated flux-surface geometry in W7-AS in the case of very high density. The benchmark tests of tools for finite-β equilibrium and power balance analysis are prerequisites for the joint profile and configuration databases for stellarators which have just been started. We have successfully recognized the compatibility of the schemes used on W7-AS and CHS. The format for the profile database is fixed by this benchmark test and will be presented elsewhere. The basis of comparative studies of MHD equilibria and diffusive transport has now been established and the next step is expected to be made efficiently.

Acknowledgement

Reference

[1]   S.P.Hirshman, W.I. van Rij, P.Merkel, Comput. Phys. Commun. **43** (1986) 143.

[2]   H.C.Howe, Oak Ridge National Laboratory Report ORNL/TM-11521 (1990).

[3]   H.Yamada et al., Nuclear Fusion **32** (1992) 25.

[4]   M.Murakami et al., in Plasma Physics and Controlled Nuclear Fusion Research (Proc. 13th Int. Conf. Washington, DC, 1990), Vol.2, IAEA, Vienna (1991) 455.

[5]   H.Yamada et al., in Controlled Fusion and Plasma Physics (Proc. 18th Eur. Conf. Berlin, 1991), Vol.15C, Part II, European Physical Society (1991) 137.

[6]   J.Geiger et al., in Controlled Fusion and Plasma Physics (Proc. 20th Eur. Conf. Lisbon, 1993), Vol.17C, Part I, European Physical Society (1993) 353.

[7]   U.Stroth et al., to appear as an IPP Report.

[8]   U.Brossmann et al., in Plasma Physics and Controlled Nuclear Fusion Research (Proc. 9th Int. Conf. Baltimore, 1982), Vol.3, IAEA, Vienna (1983) 141.

[9] K.Nishimura et al., Fusion Technol. **17** (1990) 86.

[10] A flux surface is expressed in Cartesian cylindrical coordinates R, ϕ, Z, where R is the major radius, ϕ the geometric toroidal angle and Z the distance above the midplane. When we take the corresponding flux coordinates as ρ,θ,ζ, where ρ is the flux surface label, θ is the poloidal angle, and ζ the toroidal angle, flux surfaces are defined as

$$R(\rho,\theta,\zeta) = \sum_{m,n} R_{m,n}(\rho)\cos(m\theta - n\zeta)$$

$$Z(\rho,\theta,\zeta) = \sum_{m,n} Z_{m,n}(\rho)\sin(m\theta - n\zeta)$$

$$\phi(\rho,\theta,\zeta) = \zeta$$

Shafranov shift is defined here by $(R_{0,0}(0)-R_{0,0}(1))/a$.

[11] P.Merkel, J.Comput. Phys. **66** (1986) 83.

[12] S.P.Hirshman et al., Phys. Fluids **29** (1986) 2951.

[13] K.Watanabe et al., Nucl. Fusion **32** (1992) 1499.

[14] Y.Nakamura et al., J.Phys. Soc. Jpn. **58** (1989) 3157

[15] A.H.Glasser, J.M.Greene, J.L.Johnson, Phys. Fluids **18** (1975) 875.

[16] U.Stroth et al., Nucl. Fusion **31** (1991) 2291.

[17] H.C.Howe et al., in Controlled Fusion and Plasma Physics (Proc. of 16th Eur. Conf. Venice, 1989), Vol.13B, Part II, European Physical Society (1989) 683.

[18] C.D.Beidler et al., in Controlled Fusion and Plasma Physics (Proc. 20th Eur. Conf. Lisbon, 1993), Vol.17C, Part I, European Physical Society (1993) 341.

[19] F.L.Hinton, R.D.Hazeltine, Rev. Mod. Phys. **48** (1976) 239.

Appendix

Pfirsch-Schlüter current and saddle loop measurement

Pfirsch-Schlüter current is estimated by the following simple formula for a large-aspect-ratio and axisymmetric system.

$$J_{//} = \frac{2}{\text{Y} B_0} p'(r)\cos\theta$$

(1)

It should be noted here that the pressure appearing in this formula is the average value of the perpendicular and parallel components with respect to the magnetic field line. In the W7-AS advanced stellarator, this formula is not valid. Indeed, the experiment indicates that the Shafranov shift due to Pfirsch-Schlüter currents is reduced by a factor of 2, as expected. However, the basic characteristic that the Pfirsch-Schlüter currents are proportional to the pressure gradient and inversely proportional to the rotational transform is maintained. The following argument is therefore qualitatively valid. The vertical field generated by the Pfirsch-Schlüter currents is given by,

$$B_z = \frac{\mu_0}{2\pi}(1 - \frac{r}{2R}\cos\theta)\, r^2 \cos 2\theta \cdot Y_{10}$$

where Y_{10} is the magnetic moment [a-1] defined by

$$Y_{10} = \int J_{//}\pi(R + r\cos\theta)^2 r\,d\theta\,d\,r$$

(2)

Substitution of Eq.(1) and the relation

$$<\beta> = \frac{4\mu_0 \int p(r)\,r d\,r}{B_0^2 a^2}$$

in Eq.(2) yields

$$Y_{10} = \frac{\pi R a^2}{2\mu_0} <\beta> B_0 \frac{\int p'(r)/\text{Y} \cdot r^2\,dr}{\int p(r)\,r d\,r}$$

(3)

If the rotational transform is spatially constant, the integration can be done analytically and Eq.(3) can be reduced to

$$Y_{10} = - \frac{\pi R a^2}{\mu_0 \ell} < \beta > B_0$$

(4)

As seen in Eq.(4), the vertical field is proportional to the volume-averaged β value. Saddle loop measurement of the spontaneous vertical field can therefore be directly interpreted with respect to $<\beta>$ in W7-AS because of its shearless configuration. This diagnostic is physically equivalent to the measurement of $\beta_p + l_i/2$ in tokamaks. In configurations with shear such as CHS, Eq.(2) depends on the profiles of the pressure gradient and rotational transform. For the standard configuration of CHS, the value of the integral changes from 3.1 to 4.4 when the pressure profile changes from $p=p_0(1-\rho)$ to $p=p_0(1-\rho)^3$ with the same rotational transform. That term also changes from 3.7 to 4.3 due to the finite-β effect on the rotational transform when $<\beta>$ increases from 0% to 2%. These uncertainties are greatly reduced in the W7-AS experiment. The pressure anisotropy can be discussed more accurately in combination with diamagnetic measurements which reflect the perpendicular pressure only. The precise calibration of the relation between β and the vertical field should be done with an appropriate 3-D computation such as that in the DIAGNO code [a-2].

[a-1] G.H.Neilson, J.H.Harris, Nucl. Fusion **27** (1987) 711.

[a-2] H.J.Gardner, Nucl. Fusion **30** (1990) 1417.

Figure captions

Figure 1 Shafranov shift of standard configurations in W7-AS and CHS.

Figure 2 Magnetic flux surfaces of CHS. Vacuum case. Solid lines are the case with the mode numbers m=0-3, n=-3-3, dashed and dotted lines that with m=0-7, n=-3-3.

Figure 3 Magnetic flux surfaces of W7-AS. Vacuum case. Solid lines are the case with the mode numbers: m=0-5, n=-4-4, dashed and dotted lines that with m=0-7, n=-8-8. This configuration uses only the modular coil system ($\iota \sim 0.4$).

Figure 4 Magnetic flux surfaces of W7-AS for the vacuum case. Solid lines: VMEC. Dashed and dotted lines: NEMEC.

Figure 5 Magnetic flux surfaces of W7-AS for the finite-β equilibrium with $<\beta> = 2.5\%$. Solid lines: VMEC. Dashed and dotted lines: NEMEC.

Figure 6 Shift of the magnetic axis of the W7-AS configuration with $\iota \sim 0.4$. The values are toroidally averaged.

Figure 7 Magnetic ripples with the 16th to the 20th largest components. (a) VMEC. (b) NEMEC.

Figure 8 Performance of VMEC and NEMEC in the β scan. (a) Number of iterations to get convergence. (b) Total CPU time.

Figure 9 MHD stability analysis for pressure-driven instabilities. (a) Criterion for ideal interchange mode stability (Mercier criterion). (b) Criterion for resistive interchange mode stability.

Figure 10 Measured time evolution of soft X-ray emission profile.

Figure 11 Inversion of soft X-ray profiles at 600ms. The horizontal axis is the flux-surface label. The best-fit 1-D profile is the solid curve. The measured values are plotted as circles, while the calculated values from the inverted profile are plotted as crosses. Both the measured and calculated values for each chord are plotted at the minimum flux surface along the chord. (a) With a 25 μm Be filter. (b) Without filter.

Figure 12 Benchmark test of calculation of electron thermal diffusivity. Solid lines give the results from the method employed in the analysis of W7-AS, dashed lines those from that in CHS (PROCTR). (a) Data of #18148 on W7-AS. The dotted lines show the result from the method for W7-AS with circular geometry. (b) Data of #15653 on CHS.

Figure 13 The geometrical factor for calculating the flux-surface-averaged gradients defined as $a \cdot \langle (\nabla \rho)^2 \rangle_\psi / S_\rho$ where S_ρ is the area of the flux surface. (a) W7-AS. The configuration is the same as in the benchmark test mentioned in Sec.2.2. (b) CHS. The configuration is the standard one described in Sec.2.1. The cases with $\langle \beta \rangle = 4.8\%$ in W7-AS and $\langle \beta \rangle = 1.8\%$ in CHS correspond to Shafranov shift $\Delta/a = 0.31$ and 0.41, respectively.

Figure 14 Temporal behavior of discharge #24595. For the stored energy and the line density (2mm interferometer, l=0.369m), the experimental observations and the simulation are shown by solid lines and dashes lines, respectively. They almost overlap each other. The dotted line in the stored energy is W_{sdl} from the simulation.

Figure 15 Power balance at 500ms in #24595. (a) For electrons. The dotted line is the neoclassical (Hinton-Hazeltine) heat conduction. Ionization loss is negligible in this case. (b) For ions. Charge exchange loss is negligible in this case.

Figure 16 Temporal behavior of discharge #25241. For the stored energy and the line density (HCN interferometer, l=0.528m), the experimental observations and the simulation are shown by solid lines and dashed lines, respectively.

Figure 17 Power balance at 250ms in #24595. (a) For electrons. Ionization loss is negligible in this case. (b) For ions. Charge exchange loss is negligible in this case.
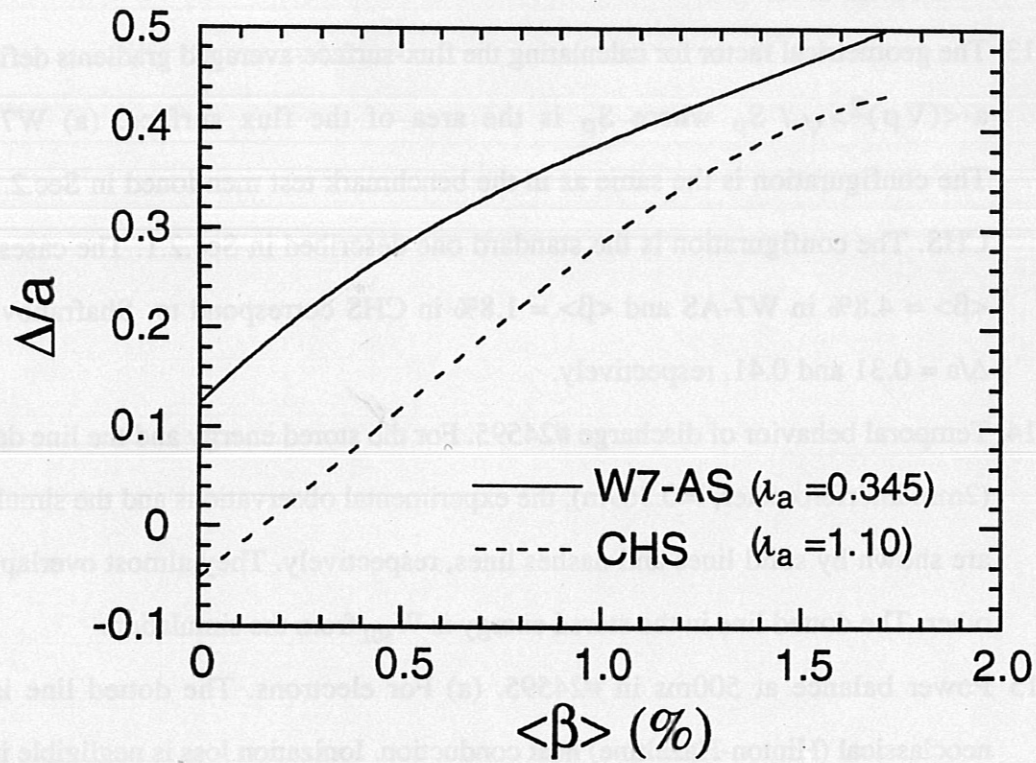
Figure 1

"Remarks on Application of VMEC and PROCTR to Wendelstein VII-AS Experiment" by H.Yamada et al.
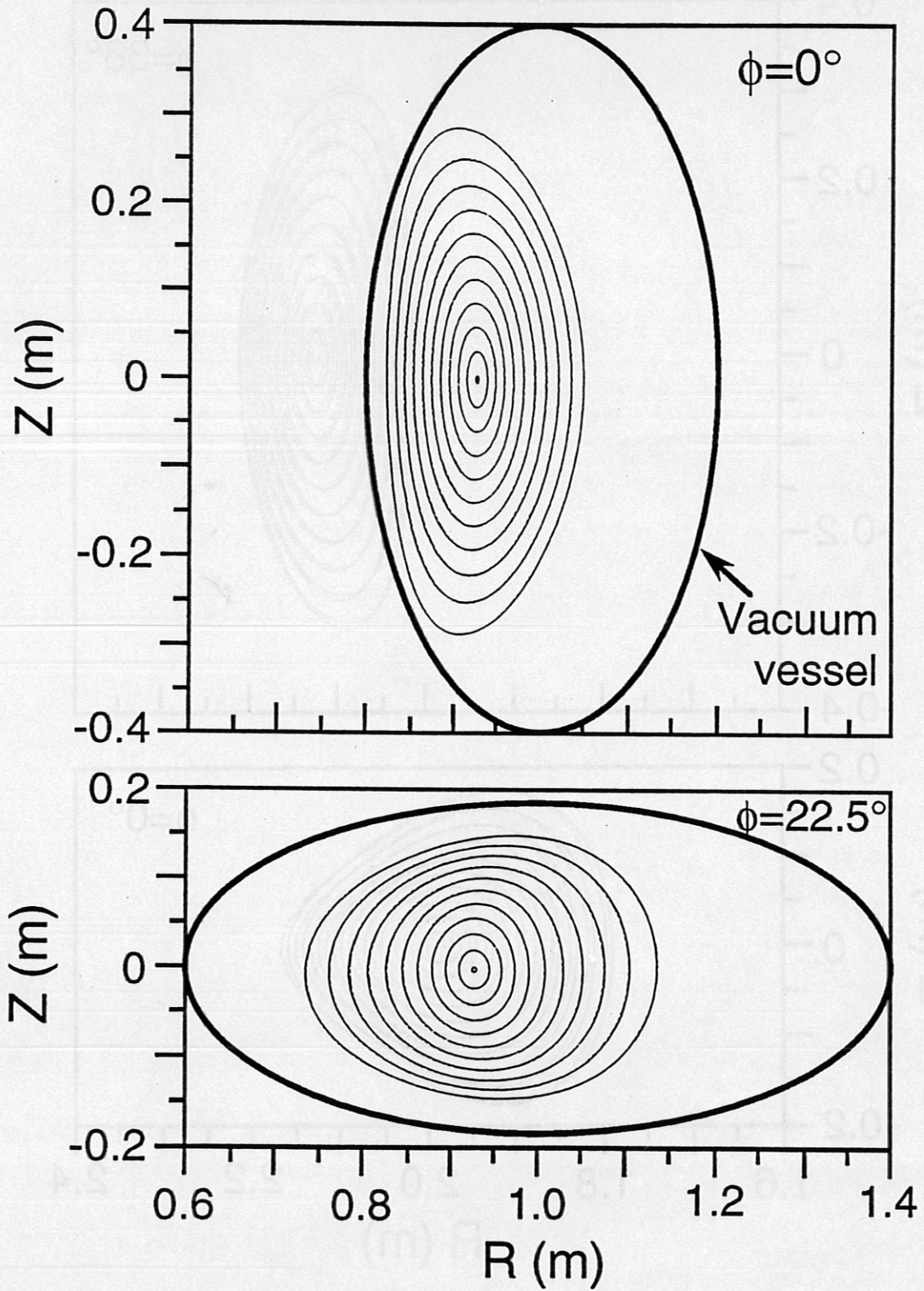
Figure 2

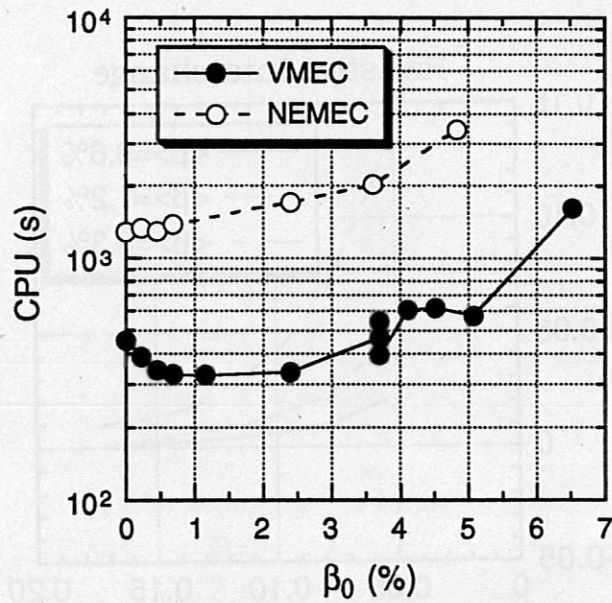"Remarks on Application of VMEC and PROCTR to Wendelstein VII-AS
Experiment" by H.Yamada et al.
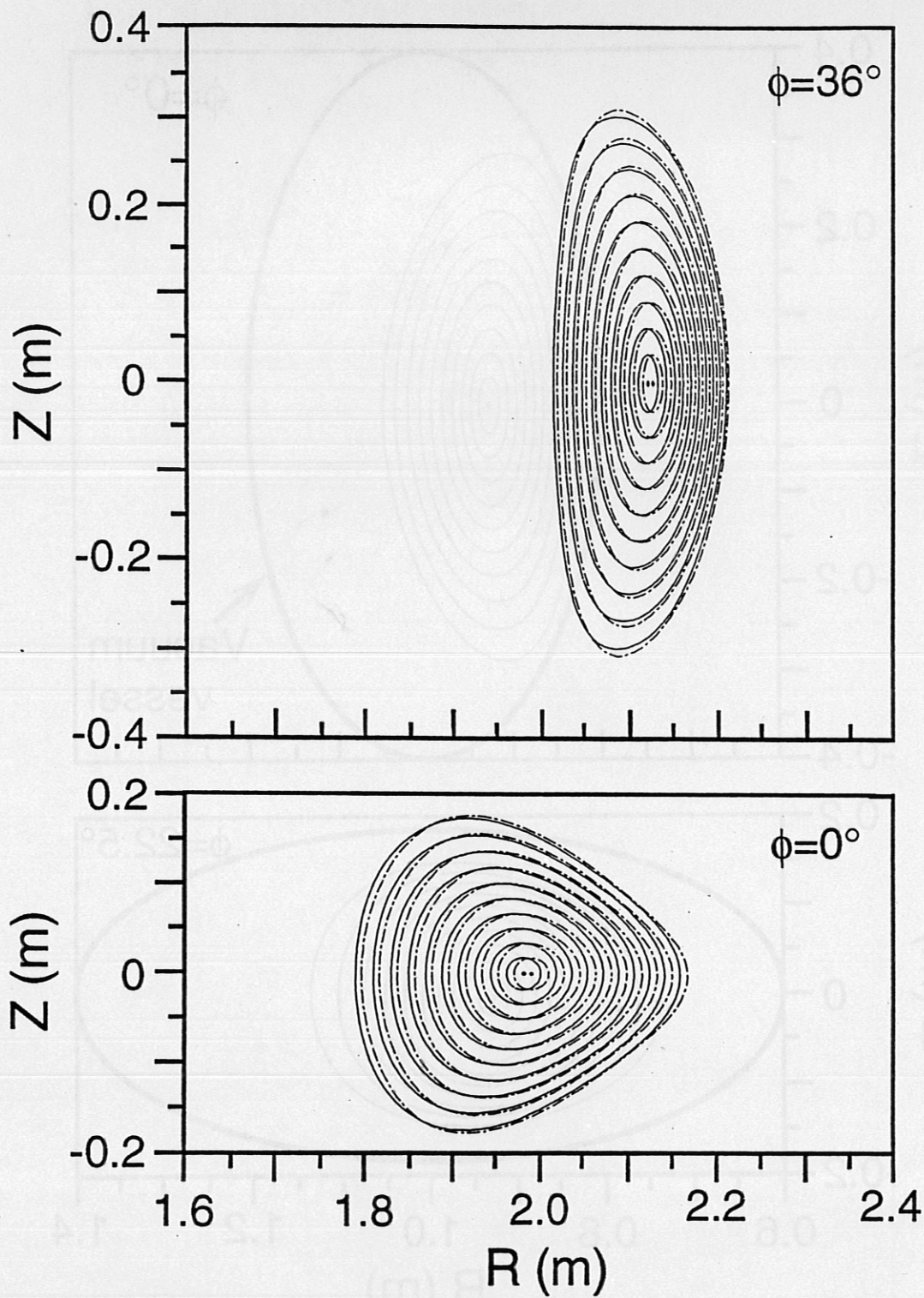
Figure 3

"Remarks on Application of VMEC and PROCTR to Wendelstein VII-AS Experiment" by H.Yamada et al.
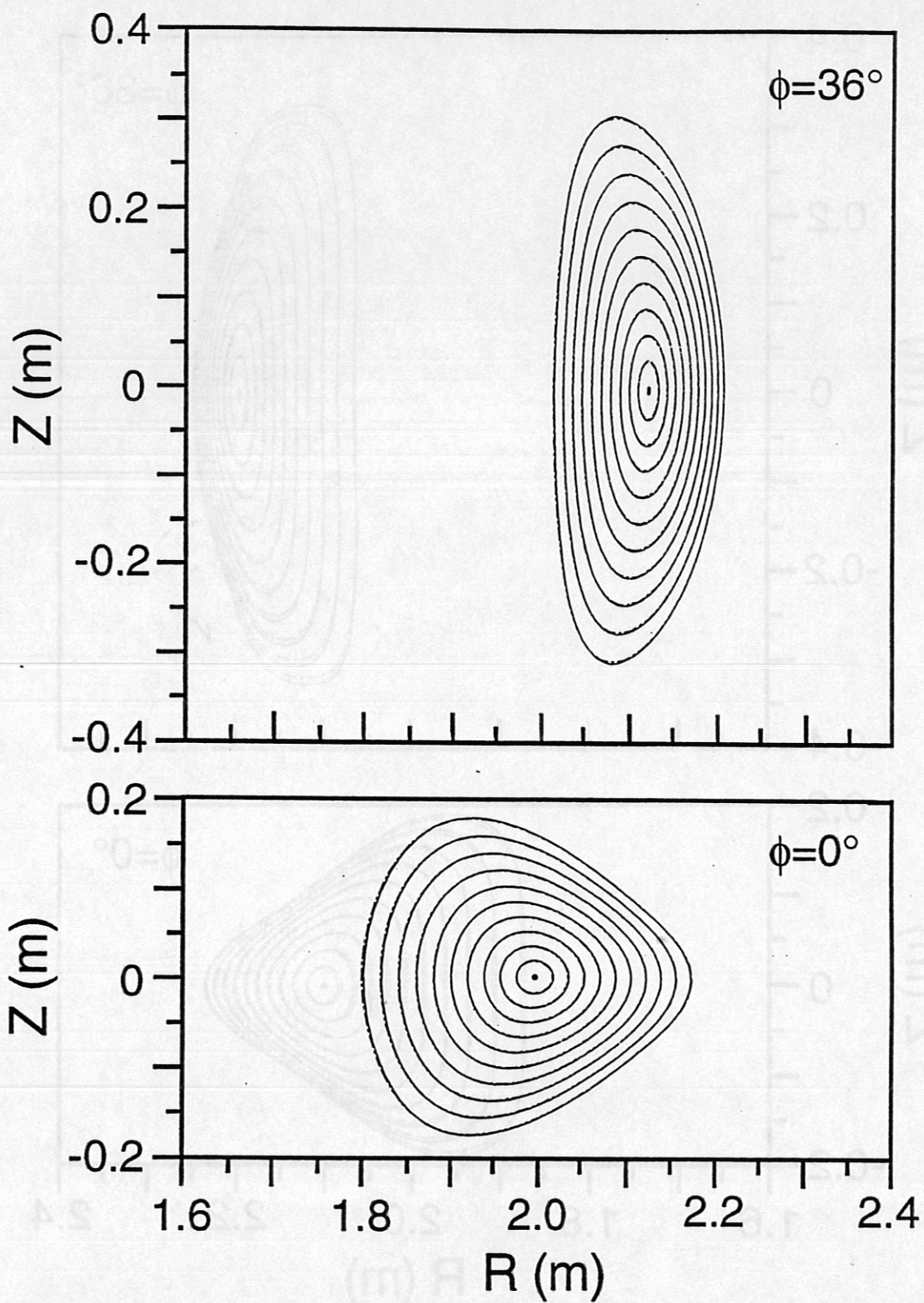
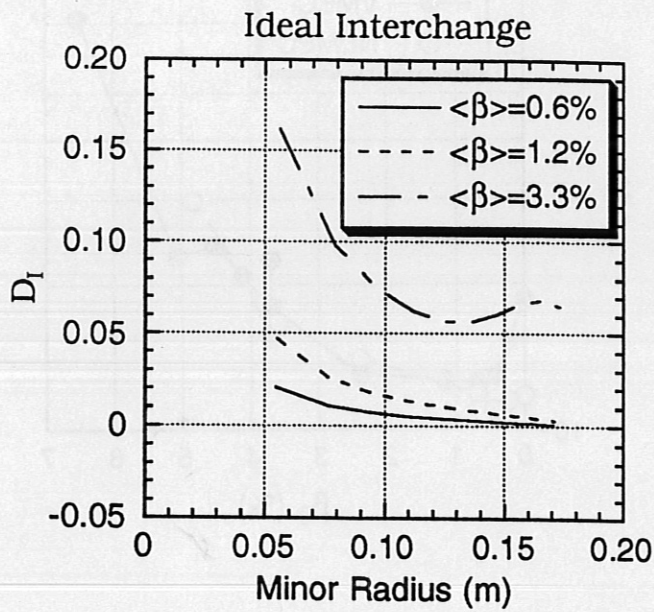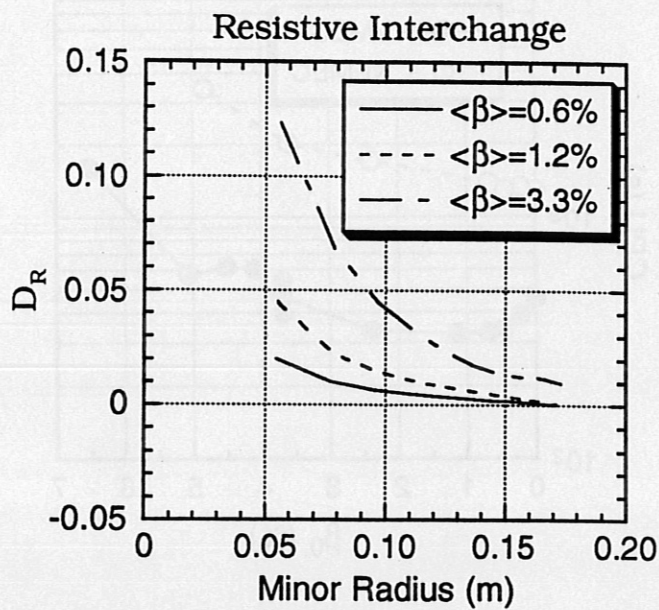Figure 4
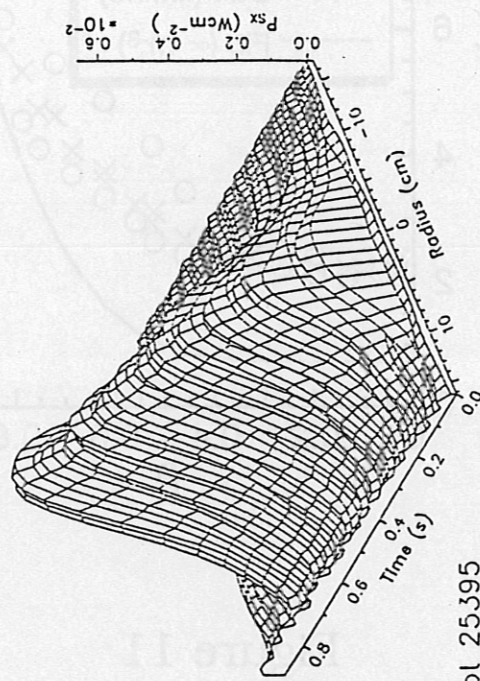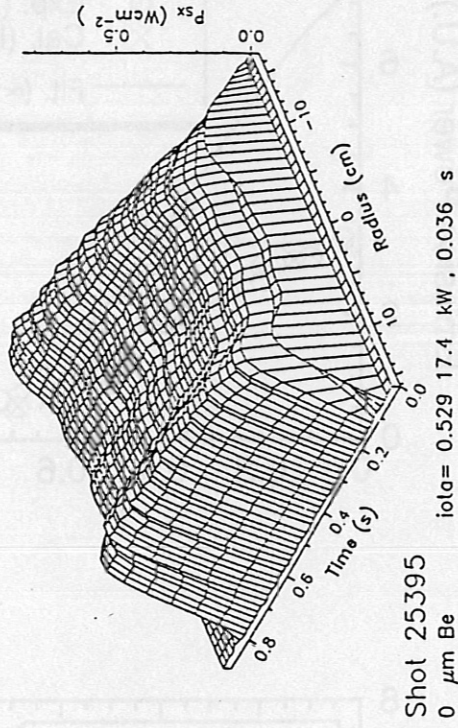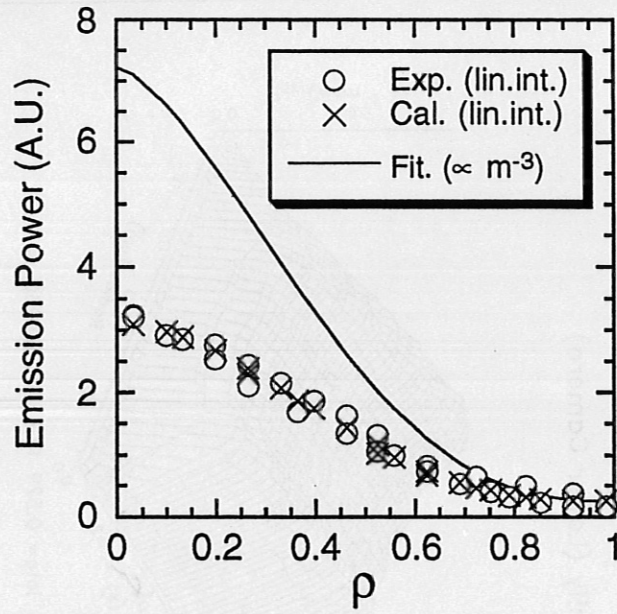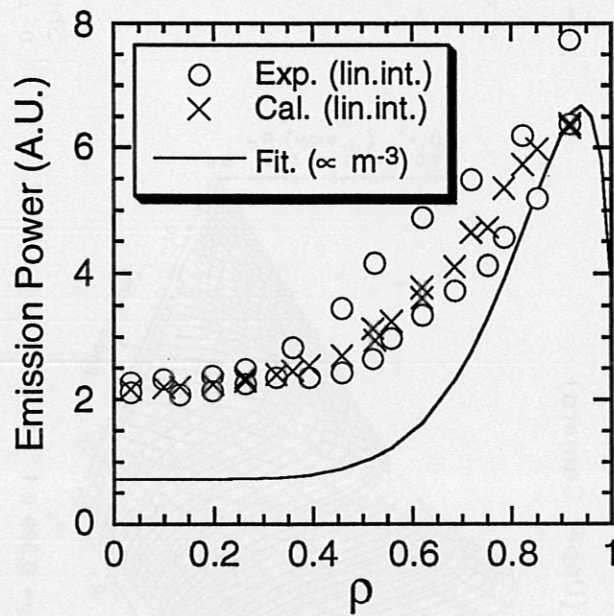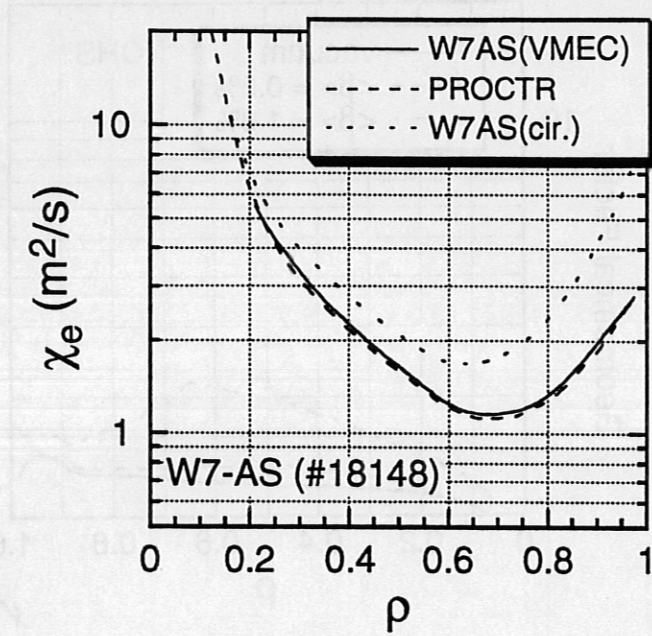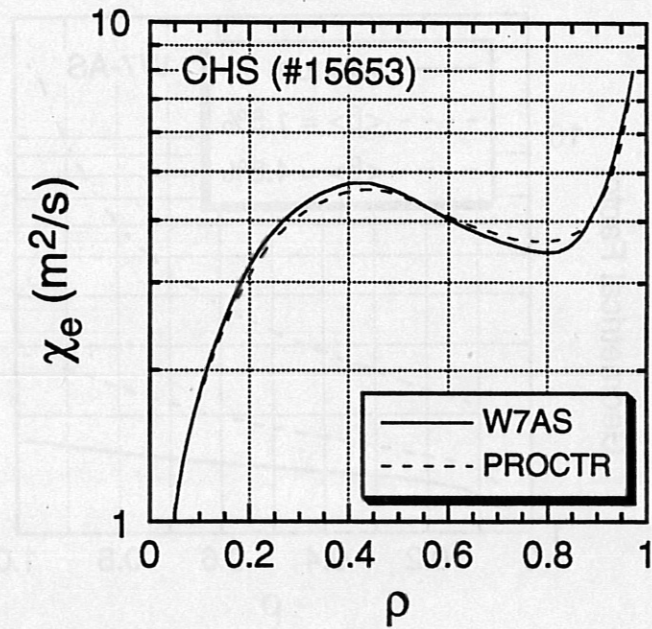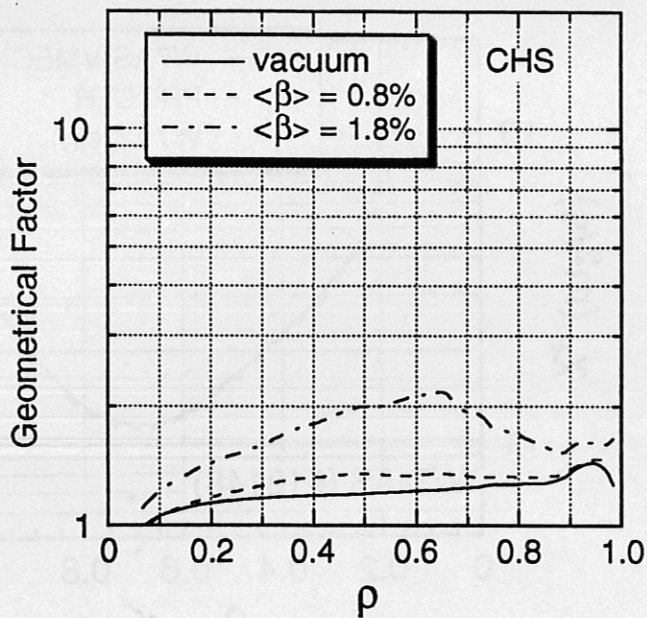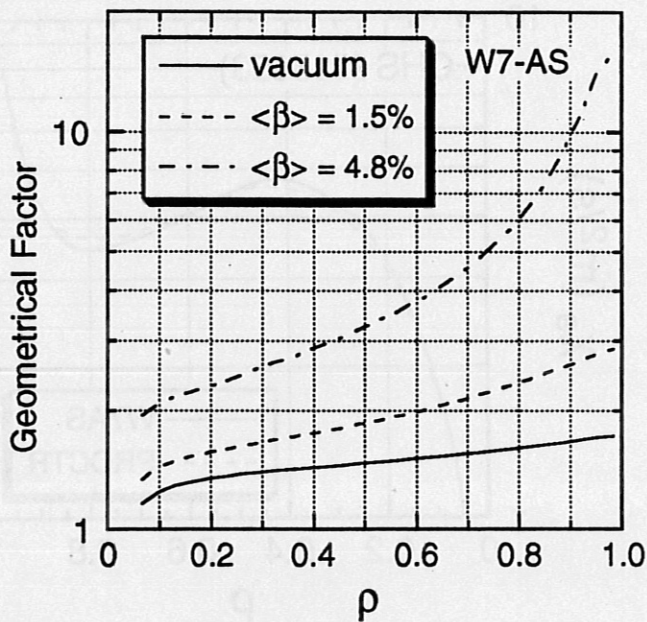
"Remarks on Application of VMEC and PROCTR to Wendelstein VII-AS Experiment" by H.Yamada et al.
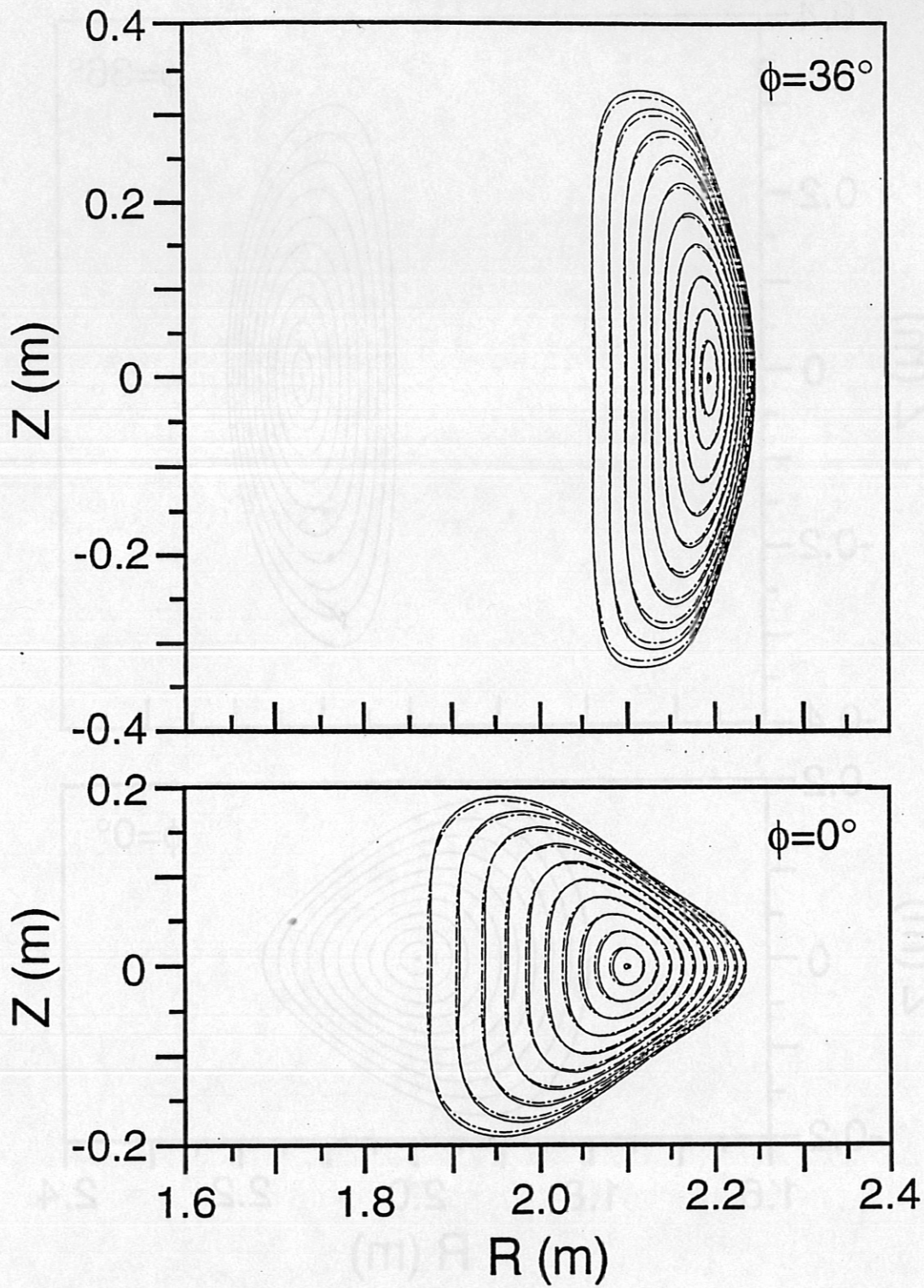
Figure 5

"Remarks on Application of VMEC and PROCTR to Wendelstein VII-AS Experiment" by H.Yamada et al.

Figure 6

$$p = p_0(1-\psi)$$
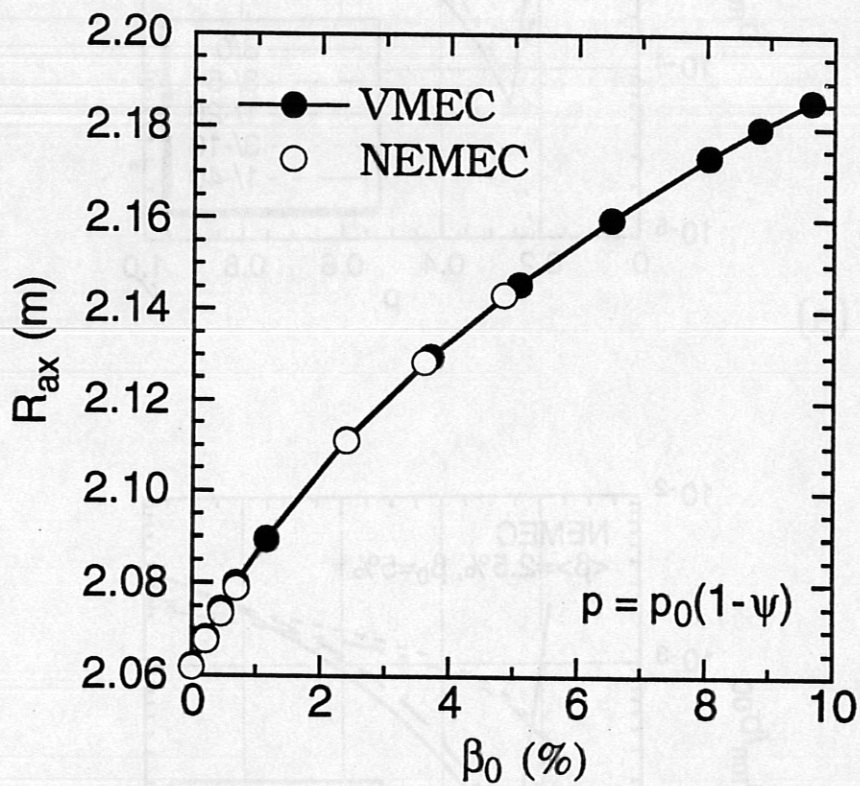
"Remarks on Application of VMEC and PROCTR to Wendelstein VII-AS Experiment" by H.Yamada et al.
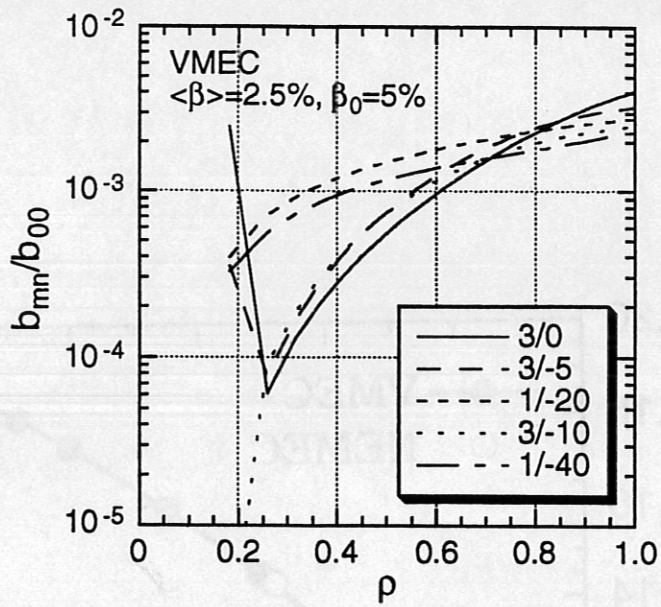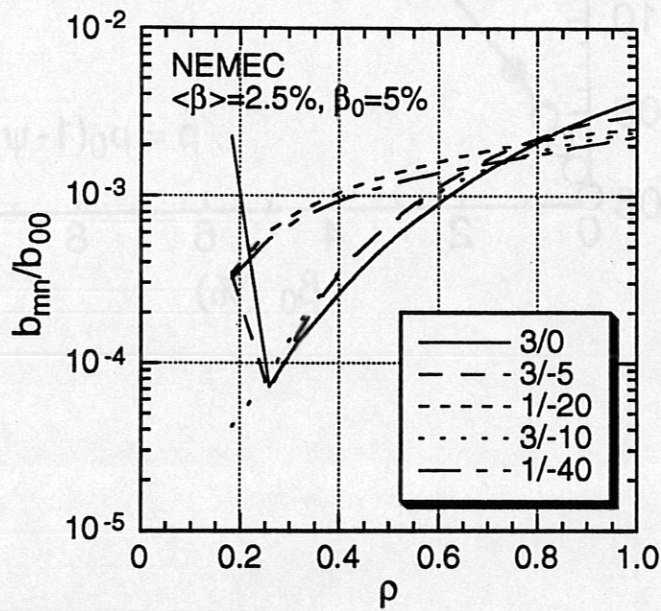
Figure 7

"Remarks on Application of VMEC and PROCTR to Wendelstein VII-AS Experiment" by H.Yamada et al.
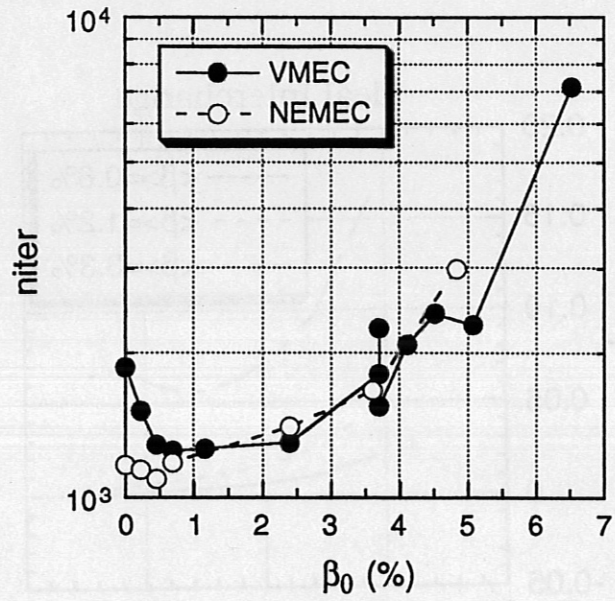
(a)

(b)

Figure 8

"Remarks on Application of VMEC and PROCTR to Wendelstein VII-AS Experiment" by H.Yamada et al.
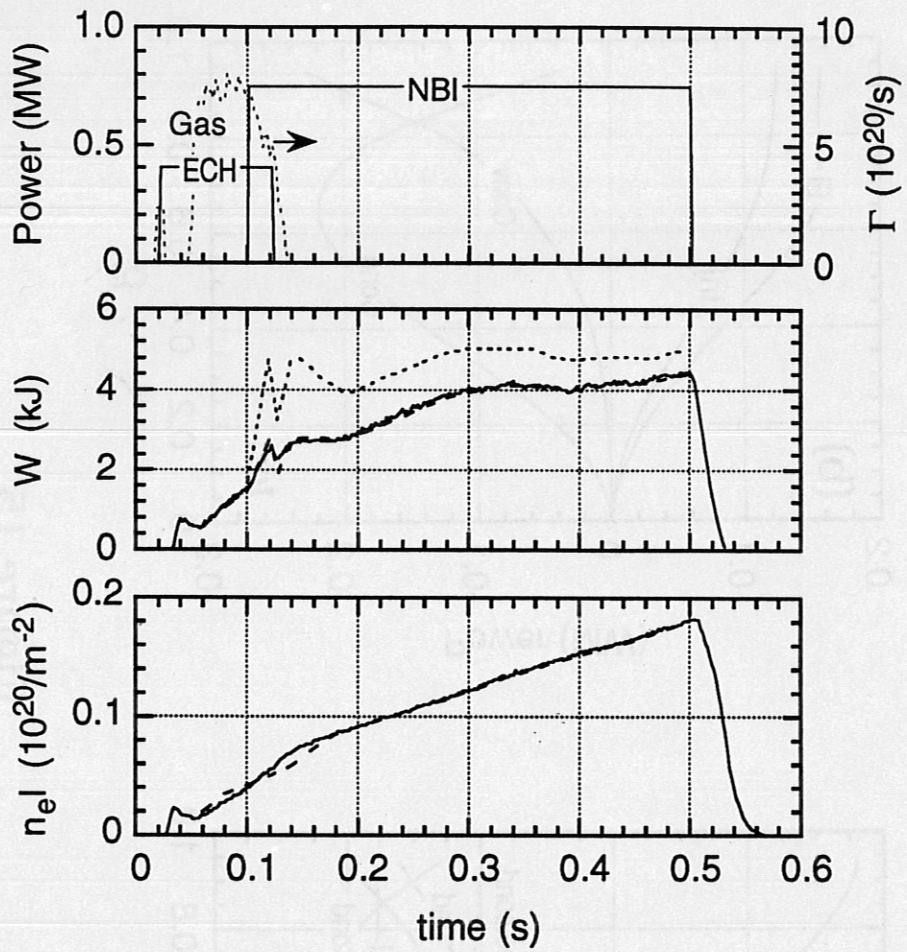
(a)

(b)

Figure 9

"Remarks on Application of VMEC and PROCTR to Wendelstein VII-AS Experiment" by H.Yamada et al.

Figure 10

"Remarks on Application of VMEC and PROCTR to Wendelstein VII-AS Experiment" by H.Yamada et al.
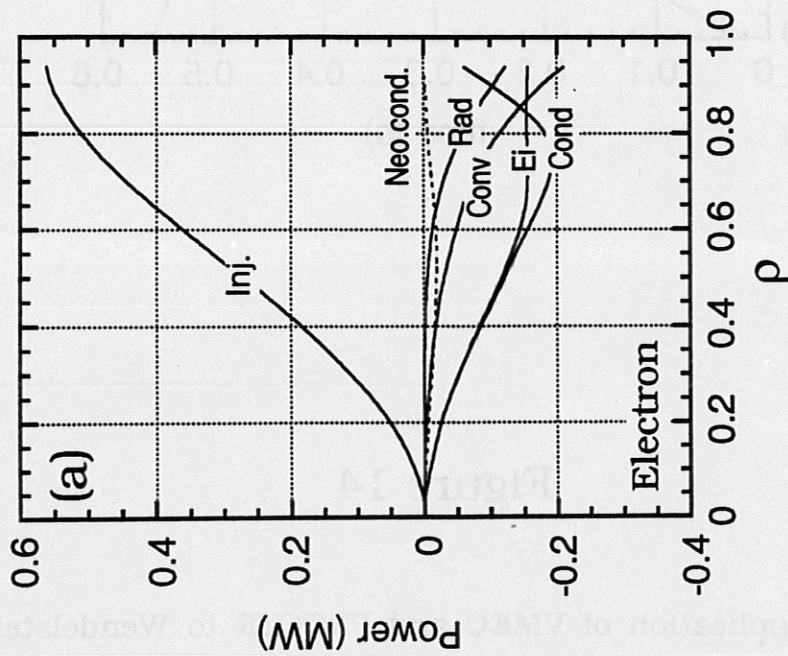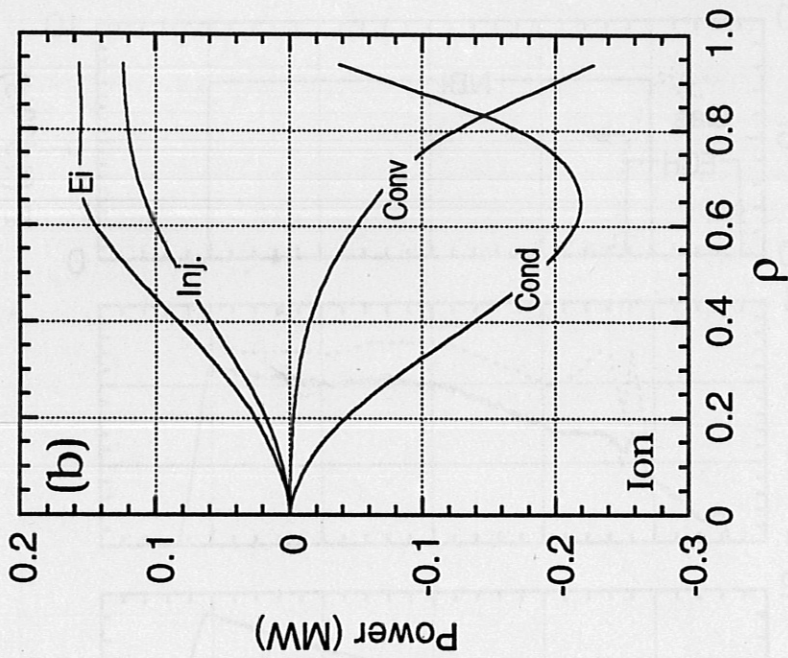
(a)

(b)

Figure 11

"Remarks on Application of VMEC and PROCTR to Wendelstein VII-AS
Experiment" by H.Yamada et al.

(a)

(b)

Figure 12

"Remarks on Application of VMEC and PROCTR to Wendelstein VII-AS
Experiment" by H.Yamada et al.

(a)

(b)

Figure 13

"Remarks on Application of VMEC and PROCTR to Wendelstein VII-AS Experiment" by H.Yamada et al.

Figure 14

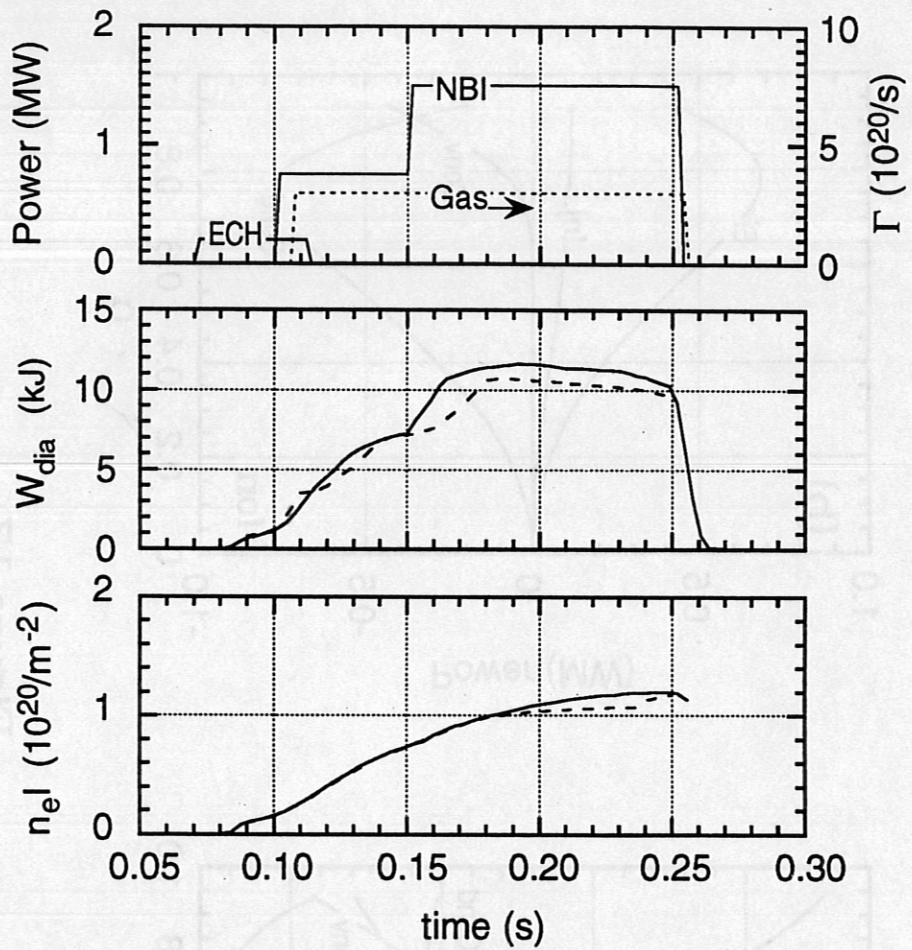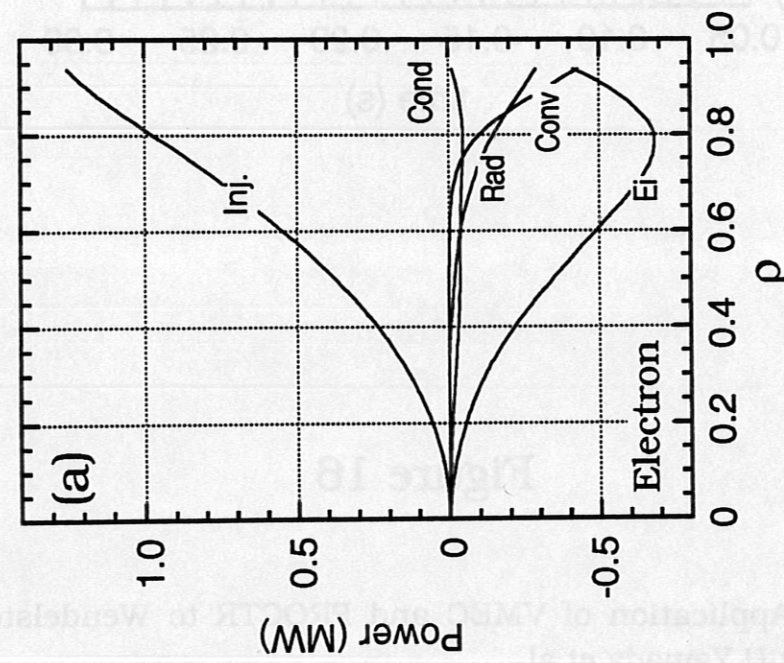"Remarks on Application of VMEC and PROCTR to Wendelstein VII-AS Experiment" by H.Yamada et al.

Figure 15

"Remarks on Application of VMEC and PROCTR to Wendelstein VII-AS Experiment" by H.Yamada et al.

Figure 16

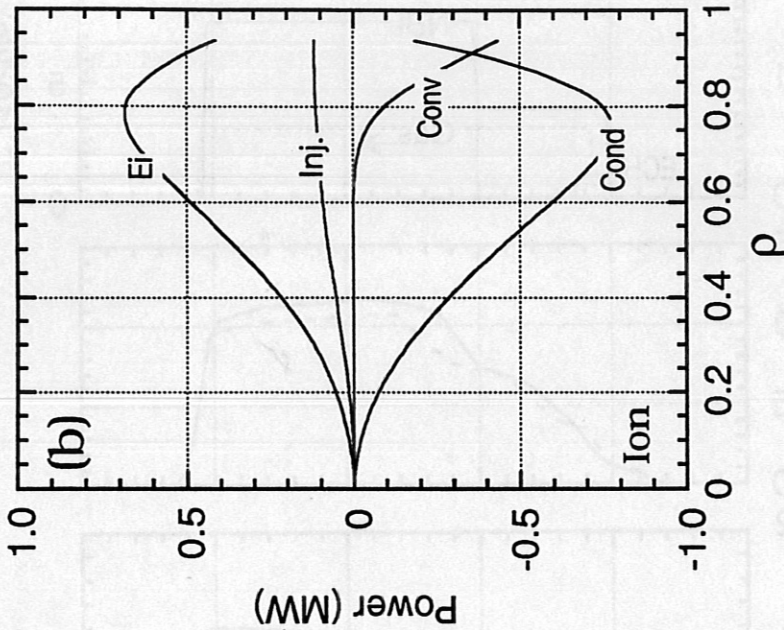"Remarks on Application of VMEC and PROCTR to Wendelstein VII-AS Experiment" by H.Yamada et al.

Figure 17

"Remarks on Application of VMEC and PROCTR to Wendelstein VII-AS Experiment" by H.Yamada et al.